

Robust Semi-Direct Monocular Visual Odometry Using Edge and Illumination-Robust Cost

Xiaolong Wu and Cédric Pradalier

Abstract—In this work, we propose a monocular semi-direct visual odometry framework, which is capable of exploiting the best attributes of edge features and local photometric information for illumination-robust camera motion estimation and scene reconstruction. In the tracking layer, the edge alignment error and image gradient error are jointly optimized through a convergence-preserved reweighting strategy, which not only preserves the property of illumination invariance but also leads to larger convergence basin and higher tracking accuracy compared with individual approaches. In the mapping layer, a fast probabilistic 1D search strategy is proposed to locate the best photometrically matched point along all geometrically possible edges, which enables real-time edge point correspondence generation using merely high-frequency components of the image. The resultant reprojection error is then used to substitute edge alignment error for joint optimization in local bundle adjustment, avoiding the partial observability issue of monocular edge mapping as well as improving the stability of optimization. We present extensive analysis and evaluation of our proposed system on synthetic and real-world benchmark datasets under the influence of illumination changes and large camera motions, where our proposed system outperforms current state-of-art algorithms.

I. INTRODUCTION

In recent decades, monocular Visual Odometry (VO) systems have shown their full potential to assist various outdoor robotic applications - from autonomous driving in urban scenes to environmental monitoring in natural environments. Among these algorithms, indirect methods [1] [2] [3] [4] are the *de facto* standards since visual features provide considerable robustness to both photometric noise and geometric distortion in images. Recent works have shown that direct methods [5] [6] [7] [8] could provide more accurate motion estimation. However, they present a much smaller convergence basin compared with indirect methods because of their loose data association.

Edge VO can be seen as a crossover of indirect and direct principles. Specifically, edges are geometric features extracted from raw images, but edge registration is performed using iterative-closest-point (ICP) based direct alignment [9]. Motion estimation using edges is particularly attractive for RGB-D VO applications for its illumination- and convergence-robustness [10] [11], while the recent development of learning-based edge detection [12] [13] opens up a new path to improve the stability of edge detection [14]. However, there are two major limiting factors of monocular edge VO: (1) the binary edge features are not self-distinguishable under ICP-based optimization framework, which makes the monocular edge mapping unstable and error-prone; (2) the accuracy of edge tracking heavily relies

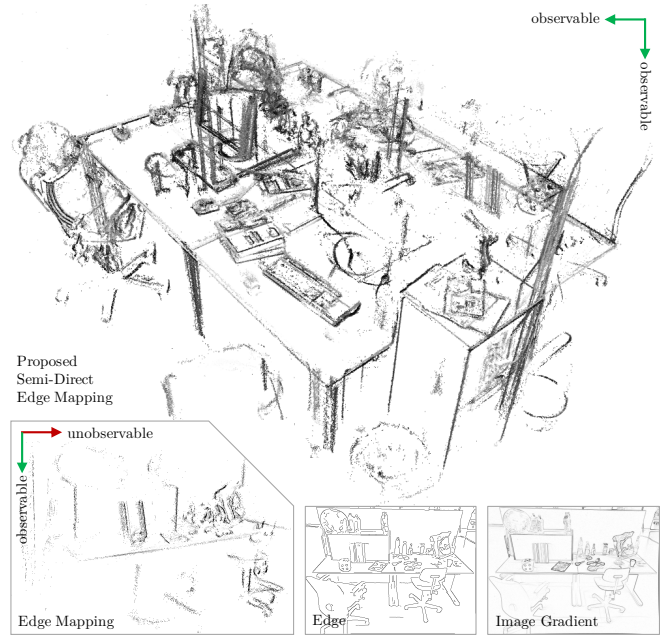


Fig. 1: Our proposed Semi-Direct Edge VO is capable of exploiting the best attributes of edge feature and image gradient to overcome the partial observability issue of pure Edge Mapping. Note that the unobservability direction is quasi-parallel with camera motion direction.

on the density of edge pixels, which degrades considerably as the edge points are sub-sampled for real-time performances.

To solve the partial observability issue, researchers have proposed to use optical flow [15] to finalize the point correspondence, which is later used to formulate reprojection error for local bundle adjustment in [16]. As for precision degradation, the combination of photometric information and edge features has been proposed to improve the tracking accuracy in [17]. However, both the standard optical flow and photometric error minimization heavily rely on brightness constancy assumption, thus limiting its usage for outdoor operations. Even if incorporating illumination-robust optical flow [18] or local photometric information [19] could serve as potential solutions, their largely reduced convergence radius is difficult to guarantee their accuracy and optimality, especially for monocular VO system where the scene points hold large depth uncertainty.

Inspired by [20] [21] [22] incorporating indirect and direct formulations, we propose a monocular semi-direct edge visual odometry framework in Fig. 1, which aims to combine the best attributes of edge features and local photometric

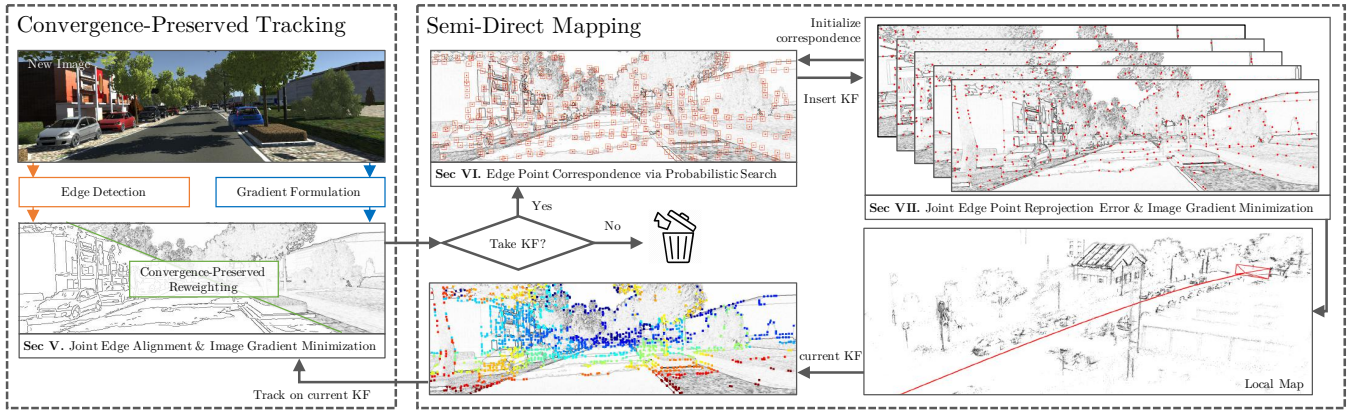


Fig. 2: Our proposed Semi-Direct Edge VO pipeline is essentially a KeyFrame (KF) based monocular VO framework.

information for illumination- and motion-robust camera pose estimation and scene reconstruction, more specifically, to solve the two issues mentioned above. The main contributions of this work are described as follows:

- A monocular semi-direct visual odometry framework that tightly couples the geometric edge feature and image gradient for illumination- and motion-robust camera motion estimation and scene reconstruction.
- A convergence-preserved reweighting strategy that is capable of preserving both large convergence basin and good final accuracy for joint optimization of the edge alignment error and local photometric error.
- A geometric error analysis and corresponding fast probabilistic 1D search strategy that can efficiently locate the best photometrically matched point along all geometrically possible edges using illumination-robust cost.

II. DIRECT AND INDIRECT IMAGE ALIGNMENT

Let us consider a reference frame, an acquired image $I_r : \Omega \rightarrow \mathbb{R}$ and its inverse depth map $D_r : \Omega \rightarrow \mathbb{R}^+$, where $\Omega \subset \mathbb{R}^2$ is the image domain. A 3D scene point $\mathbf{P} = (x, y, z)^T$ is parameterized by its inverse depth $d = z^{-1}$ in the reference frame instead of the conventional 3 unknowns. Each pixel in the reference frame $\mathbf{p} = (u, v)^T \in \Omega$ can be back-projected into 3D world using the back-projection function $\mathbf{P} = \pi^{-1}(\mathbf{p})$. Inversely, the 3D projective warp function $\mathbf{p} = \pi(\mathbf{P})$ can project 3D point onto image space.

A 3D rigid body transformation $\mathbf{G} \in SE(3)$ can be generally divided into a 3D rigid body rotation $\mathbf{R} \in SO(3)$ and translation $\mathbf{t} \in \mathbb{R}^3$. In the optimization framework, \mathbf{G} is represented as its corresponding Lie Group component $\xi \in \mathfrak{se}(3)$, where this element can be mapped to $\mathbf{G} \in SE(3)$ through the exponential mapping described in [23].

Given arbitrary pixel selector $S(\cdot)$, the group of edge pixels S_r extracted from the reference image can be expressed as:

$$S_r = \{\mathbf{p}_r\} = S(I_r) \quad (1)$$

Each selected pixel $\mathbf{p}_r \in S_r$ are subsequently projected to current frame k as:

$$\mathbf{p}_{kr} = \pi(\mathbf{R}_{kr}\pi^{-1}(\mathbf{p}_r, D_r(\mathbf{p}_r)) + \mathbf{t}_{kr}) \quad (2)$$

The generalized photometric error $E_{kr}^{\mathcal{P}}$, edge alignment error $E_{kr}^{\mathcal{E}}$, and reprojection error $E_{kr}^{\mathcal{R}}$ from reference frame to frame k can be generally written as:

$$E_{kr}^{\mathcal{P}} := \sum_{\mathbf{p}_r \in S_r^{\mathcal{P}}} w_{\mathbf{p}_r} \|F_k(\mathbf{p}_{kr}) - F_r(\mathbf{p}_r)\|_{\gamma} \quad (3)$$

$$E_{kr}^{\mathcal{E}} := \sum_{\mathbf{p}_r \in S_r^{\mathcal{E}}} w_{\mathbf{p}_r}^{\mathcal{E}} \|\mathbf{p}_{kr} - n(\mathbf{p}_{kr})\|_{\gamma} \quad (4)$$

$$E_{kr}^{\mathcal{R}} := \sum_{\mathbf{p}_r \in S_r^{\mathcal{R}}} w_{\mathbf{p}_r}^{\mathcal{R}} \|\mathbf{p}_{kr} - \mathbf{p}_k\|_{\gamma} \quad (5)$$

where $w_{\mathbf{p}_r}$ is the weight assigned for each selected pixel from S_r in reference frame, and $\|\cdot\|_{\gamma}$ is the Huber norm. Specifically for each formulation, $F(\cdot)$ represents any representation calculated from Image I , such as intensity, gradient or some dense descriptors, $n(\mathbf{p}_{kr})$ represents the nearest neighbor of the projected edge pixel \mathbf{p}_{kr} in current frame k using the Euclidean distance metric, $\{\mathbf{p}_r, \mathbf{p}_k\}$ is a pair of matched points between reference image and image k .

III. SYSTEM OVERVIEW

Fig. 2 illustrates our proposed semi-direct VO framework, which consists of two parallel threads named convergence-preserved tracking and semi-direct mapping threads. Our proposed tracking layer in Sec. IV is in charge of coarsely estimating the camera motion from current frame to current keyframe based on the already reconstructed local maps and camera motion model, while the mapping layer refines the point correspondences in Sec. V and jointly optimizes the camera poses and scene structure within a sliding window of keyframes for further refinement in Sec. VI. To gain the illumination-robustness, our proposed system combines the edge feature and image gradient magnitude instead of standard point feature and pixel intensity.

IV. CONVERGENCE-PRESERVED TRACKING

In this section, we detail our proposed convergence-preserved tracking algorithm, which minimizes dynamically reweighted edge alignment error and image gradient error for illumination-robust motion estimation. More specifically, we present the two primary components of our proposed

tracking algorithm: joint optimization framework IV-A and convergence-preserved reweighting strategy IV-B.

A. Joint Optimization

Our proposed camera motion tracking algorithm is essentially a joint optimization framework, where the edge alignment error in Eqn. 4 and generalized photometric error in Eqn. 3 are minimized altogether to get an optimal relative pose through optimization in Lie-Manifold. Mathematically, the combined energy function can be written as:

$$\xi_{kr}^* := \underset{\xi_{kr}}{\operatorname{argmin}} \left(E_{kr}^{\mathcal{E}}(\xi_{kr}) + \alpha\beta E_{kr}^{\mathcal{P}}(\xi_{kr}) \right) \quad (6)$$

where α is a constant balancing factor that adjusts the two energies to similar scales, β is a dynamic balancing factor between combined energies that play an essential role for convergence-preserved reweighting. Both energy functions in Eqn. 4 and 3 are weighted by the inverse variance of the inverse depth of selected points, which can be written as:

$$w_{\mathbf{p}_r}^{\mathcal{E}} = w_{\mathbf{p}_r}^{\mathcal{P}} = \frac{1}{\sigma_{d^{-1}}^2} \quad (7)$$

For illumination invariance, the image gradient magnitude is chosen based on the analysis [19] for local photometric error formulation, which can be expressed as $F(\cdot) := \|\nabla I(\cdot)\|_2$ in Eqn. 3. To stabilize the image alignment, the image gradient costs in a small patch centered at the point of interest are aggregated, where the depth of central point is fixed for all pixels in the patch for optimization.

B. Convergence-Preserved Reweighting

In Fig. 3, the energy of edge alignment shows favorable convergence basin for optimization. However, it holds multiple local minima around the global optimal due to pixel sub-sampling. In contrast, image gradient cost shows clear global optimal under point decimation but holds a much smaller convergence basin. Simply averaging of two distinct energy functions for optimization may both deteriorate convergence basin and tracking accuracy. To preserve both large convergence basin and final accuracy, a weighting factor β in Eqn. 6 and a convergence-preserved reweighting strategy are introduced into our proposed algorithm, which is capable of dynamically adjusting importance factors between edge and image gradient energies during joint optimization.

The key idea behind the convergence-preserved reweighting strategy is to exploit our prior knowledge about convergence basin and final accuracy of each method, assigning more weights on energy with large convergence radius at the beginning of optimization and gradually increasing the weights for energy with high tracking accuracy but small convergence basin. More specifically, β is initialized as 0, which means total reliance on edge alignment for convergence. Once the combined energy arrives at local minima, β is increased at pre-defined steps for the next iteration until arriving at its upper limit. In practice, both the steps and upper limits of β are set by trial and error for the trade-off between accuracy and efficiency.

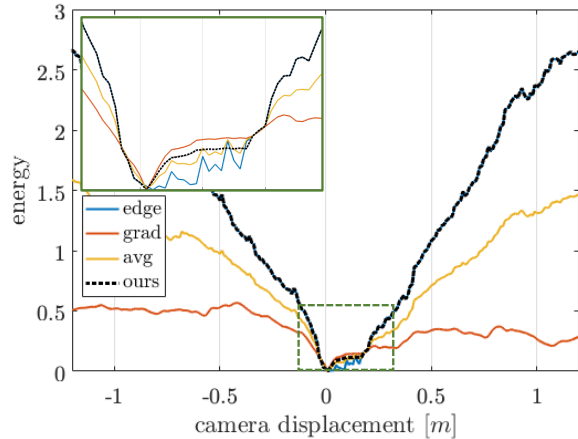


Fig. 3: **Energy comparison** of edge alignment, image gradient, simple average, and our proposed convergence-preserved algorithm.

V. EDGE POINT CORRESPONDENCE

In this section, we present our proposed edge point correspondence initialization and refinement methods, which is essentially an exhaustive search method for the gradient-difference-minimization point along with local edge points. For fast implementation, the search region is defined by geometric uncertainty analysis. The necessity of edge point correspondence refinement roots from the fact that the edge pixel matches from either edge tracking (\diamond) or edge mapping (\square) cannot guarantee the correctness of point correspondences (\circ) as shown in Fig. 4 (Left). In general, the larger the angle θ between Epipolar line \mathbf{l} and local edge pixel gradient direction \mathbf{g} , the higher the potential mismatches are, which can be captured by geometric uncertainty analysis.

A. Geometric Uncertainty Analysis

To realize the potential search region for edge point refinement, the geometric error is defined as the error variance on search radius along edge direction, which is mainly caused by tracking error on ξ and inverse depth error on d . To simplify the analysis, we make two assumptions: (1) the edgelet is locally linear and its gradient direction is locally constant, (2) the rotation error on ξ plays a minor role for Epipolar line direction estimation. After such simplifications, the search line along edge direction S and Epipolar line can be approximated as:

$$S := \{\mathbf{p}^* + \lambda \mathbf{g}_\perp\} \quad L := \{\mathbf{p}_0 + \mu \mathbf{l}\} \quad (8)$$

where \mathbf{p}_0 represents the reprojected edge point, and \mathbf{p}^* denotes an edge point correspondence lying on the locally linear region. \mathbf{g}_\perp and \mathbf{l} are the normalized perpendicular Epipolar line and image gradient directions, while λ and μ are their distance factors. The intersection between two lines $S \cap L$ can be expressed as:

$$\mathbf{p}^* + \lambda \mathbf{g}_\perp = \mathbf{p}_0 + \mu \mathbf{l} \quad (9)$$

where the geometric relationship is illustrated in Fig. 4 (Middle).

Eliminating the Epipolar distance factor μ , the true search radius can be expressed as:

$$\lambda(\mathbf{p}_0) = \frac{\langle \mathbf{p}_0 - \mathbf{p}^*, \mathbf{l}_\perp \rangle}{\langle \mathbf{g}, \mathbf{l} \rangle} \quad (10)$$

By making additional assumption that \mathbf{p}_0 is the only variable and subject to Gaussian noise, we can perform uncertainty propagation, where the variance of geometric search radius variance can be derived as:

$$\sigma_\lambda^2 = \mathbf{J}_\lambda \sigma_{\mathbf{p}_0}^2 \mathbf{J}_\lambda^T = \frac{\sigma_{\mathbf{p}_0}^2}{\langle \mathbf{g}, \mathbf{l} \rangle^2} = \frac{\sigma_{\mathbf{p}_0}^2}{\cos^2 \theta} \quad (11)$$

where \mathbf{J}_λ is the Jacobian of Eqn. 10 w.r.t. λ , θ represents the angle between the normalized image gradient and Epipolar line vectors, and $\sigma_{\mathbf{p}_0}^2$ denotes the variance of reprojected point.

It should be noted that $\sigma_{\mathbf{p}_0}$ is jointly affected by the uncertainty of depth estimate d and erroneous camera motion ξ . For simplicity, we assume the uncertainties of d and ξ are independent, so that the upper bound of variance can be estimated using inequality relationship as:

$$\sigma_{\mathbf{p}_0(\xi, d)} = \|\sigma_{\mathbf{p}_0(\xi)}^2 + \sigma_{\mathbf{p}_0(d)}^2\|^{\frac{1}{2}} \leq \sigma_{\mathbf{p}_0(\xi)} + \sigma_{\mathbf{p}_0(d)} \quad (12)$$

Setting the center of search to be the temporally estimated edge point correspondence $n(\mathbf{p}_0(d, \xi))$, the search region can be expressed as:

$$\lambda \in \left(-\frac{\sigma_{\mathbf{p}_0(\xi)} + \sigma_{\mathbf{p}_0(d)}}{|\cos \theta|}, \frac{\sigma_{\mathbf{p}_0(\xi)} + \sigma_{\mathbf{p}_0(d)}}{|\cos \theta|} \right) \quad (13)$$

where the search direction can be arbitrarily defined due to the symmetry. Fig. 4 (Right) indicates the resultant search region, where the region caused by uncertainty of ξ is colored as orange and error of d as blue.

For fast implementation, we propose to use one-point variance to approximate the upper bound of $\sigma_{\mathbf{p}_0(\xi)}$ instead of sophisticated analytic uncertainty propagation, which is calculated by assuming that mismatch error is totally caused by the uncertainty of camera motion estimate as:

$$\sigma_{\mathbf{p}_0(\xi)} := \gamma \|\mathbf{p}_0(d, \xi) - n(\mathbf{p}_0(d, \xi))\|_2 \quad (14)$$

where the temporal edge point correspondence $n(\mathbf{p}_0(d, \xi))$ serves as ground truth match and the enlargement factor γ is introduced to compensate the potential shrink of search radius due to false ground truth assumption. Unlike $\sigma_{\mathbf{p}_0(\xi)}$ requiring hard-to-estimate uncertainties for propagation, the depth variance σ_d is maintained during tracking and mapping, which simplifies the variance approximation as:

$$\sigma_{\mathbf{p}_0(d)} := \frac{\mathbf{p}_0(d + \sigma_d, \xi) - \mathbf{p}_0(d - \sigma_d, \xi)}{2} \quad (15)$$

B. Probabilistic 1D Search

Given camera transformations between keyframes within a sliding optimization window, all mapped edge points hosted in different keyframes are projected onto newly added keyframe. Their nearest neighbors in new keyframe then serve as the coarse initialization of edge point correspondence for further refinement. Our proposed search strategy

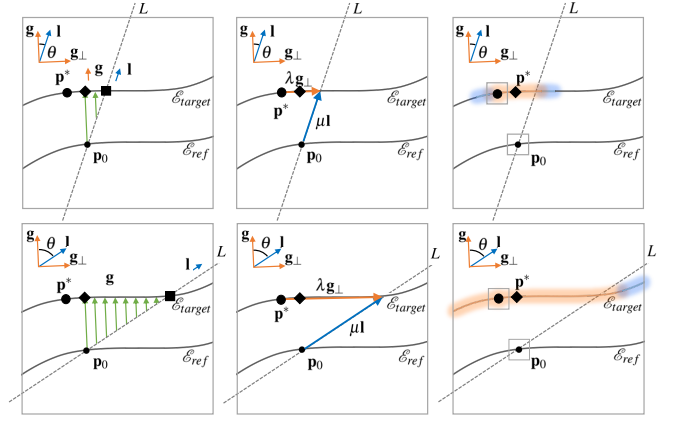


Fig. 4: **Point correspondence refinement** for edge point with small (Top) and large (Bottom) θ . Left: the edge point matches from tracking and pure edge mapping layer. Middle: the geometric relationship involved in search region derivation. Right: the resultant search region and patch-based matching.

starts with the coarsely estimated edge point correspondence. A standard region growing algorithm is used to explore the nearby edge points for matching, where the growth time is defined in Eqn. 13. At each iteration, the template-based matching is performed through estimating the image gradient magnitude difference of a 5x5 patch between the query and the target edge points in Fig. 4 (Right). The search stops at either maximum growth boundary or discontinuity of edges, where the edge point generating smallest error is chosen as the best match for local bundle adjustment. The uncertainty of estimated correspondence σ_{c-1}^2 is calculated as their matching error for consistency.

VI. LOCAL BUNDLE ADJUSTMENT

Our proposed local bundle adjustment algorithm is still a joint optimization framework, where the edge point correspondence error in Eqn. 5 and generalized photometric error in Eqn. 3 are minimized altogether to optimize the relative camera poses and local scene structure jointly. Mathematically, the combined energy function can be written as:

$$\xi_{kr}^*, d_r^* := \operatorname{argmin}_{\xi_{kr}, d_r} \sum_{k, r \in S_w} E_{kr}^{\mathcal{R}}(\xi_{kr}, d_r) + \alpha E_{kr}^{\mathcal{P}}(\xi_{kr}, d_r) \quad (16)$$

where α is a constant balancing factor same as Eqn. 6. The energy function in Eqn. 5 is weighted by the point correspondence uncertainty, while the energy in Eqn. 3 is still weighted by the inverse variance of the inverse depth of selected points, which can be written as:

$$w_{\mathbf{p}_r}^{\mathcal{R}} = \frac{1}{\sigma_c^2} \quad w_{\mathbf{p}_r}^{\mathcal{P}} = \frac{1}{\sigma_{d-1}^2} \quad (17)$$

Similar to the tracking algorithm, the image gradient magnitude is also chosen for local photometric error formulation, where the image patch is used for optimization stabilization.

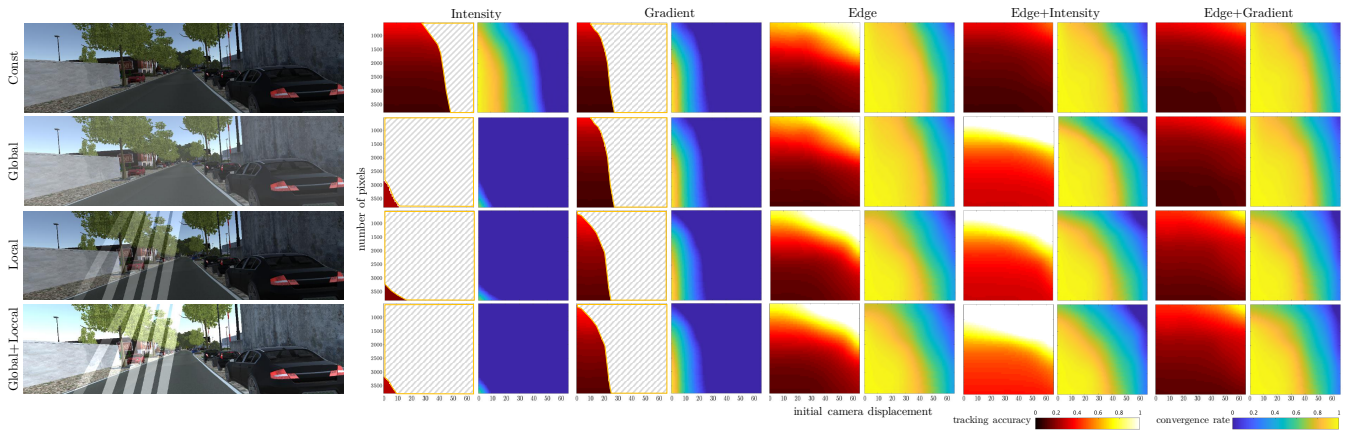


Fig. 5: **Evaluation on tracking** Left: the example images with simulated illumination changes. Right: the final tracking accuracy and convergence rate are plotted versus initial pose displacement and amount of selected pixels under global or/and local illumination changes. Note that both *Edge+Intensity* and *Edge+Gradient* implement our proposed convergence-preserved reweighting strategy. The white patterned area indicates that the data is unreliable since the convergence rate is lower than 30% .

VII. EVALUATION

In this section, we evaluate our proposed semi-direct edge VO system quantitatively on publicly available datasets [24] [25] [26] using real-time capable edge detectors [31] [12] [13]. Compared to other edge VO systems concentrating on the indoor navigation, our evaluation mainly focuses on challenging outdoor environments, where the sun-glare and pixel over-exposure are main factors of tracking failure.

A. Evaluation on Convergence-Preserved Tracking

First of all, we evaluate the convergence basin and accuracy of our proposed convergence-preserved tracking against initial camera displacement and amount of selected pixels, where the convergence rate and final tracking accuracy after convergence are set as metrics for quantitative analysis. A photo-realistic vKITTI [24] dataset with simulated global illumination bias or/and solar-glare patterned local lighting changes is used to evaluate our proposed approach quantitatively.

In Fig. 5, we can summarize three observations: (1) The *gradient* approach shows good tracking accuracy under point decimation against both global and local illumination changes but holds a significantly small convergence basin. (2) Both the convergence basin and tracking accuracy of *edge* method are both affected by local illumination changes and pixel sub-sampling, where the pixel sub-sampling plays a major role. (3) Our proposed convergence-preserved reweighting approach outperforms other strategies, which can lead to both good tracking accuracy as *gradient* method and large convergence basin as *edge* approach under pixel selection.

B. Evaluation on Illumination and Motion Robustness

The overall system performance of our proposed semi-direct VO algorithm is evaluated using Symphony Lake [25] dataset, which consists of millions of natural lakeshore images heavily contaminated by (1) smooth (auto-exposure)

and (2) sudden (sun-glare) lighting changes, as well as (3) the tree-sky boundary pixel over-exposure. Unlike sun-glare that randomly occurs in sunny days of a year, the over-exposure induced appearance changes show significant variations across seasons. In general, the denser the leaves (Summer), the fewer boundary pixels are 'eaten' by lights, the VO system is, therefore, less affected by over-exposure, and vice versa (Winter). Based on these observations, we choose 12 surveys (3 surveys per season) that are heavily contaminated with sun-glare and categorize results based on seasons. For motion robustness evaluation, we down-samples the selected sequences at a sample rate of 3 for fast camera motion simulation. For quantitative analysis, the ground truth poses is calculated through Laser-GPS-based global pose graph optimization described in [28]. The scale of trajectory from monocular VO are corrected using ground truth poses at every 200 frames, while the loop-closure functionality is disabled for ORBSLAM2 for a fair comparison.

In Fig. 6, the pointclouds show that our proposed approach is capable of reconstructing high-quality human-made structures as well as the natural scenes under illumination contamination. Comparing reconstruction results across seasons, we can observe the structural changes of trees between different times of the year. A more detailed quantitative evaluation concerning relative pose errors (RPEs), failure rate, and runtime performance using complete and down-sampled sequences are presented in Table. I. The camera pose error within tracking failure locations is calculated using pre-defined maximum tracking error (30.0 cm/m), where the large errors indicate both low tracking accuracy and low completion rate. The major causes of tracking failure of the current state-of-art methods are analyzed in our previous work [29].

In general, our proposed approach outperforms all other state-of-art methods, where the minimum performance boosts show in *Summer* while the maximum ones in *Winter*. Such variation can be attributed to the fact that the *Winter* images

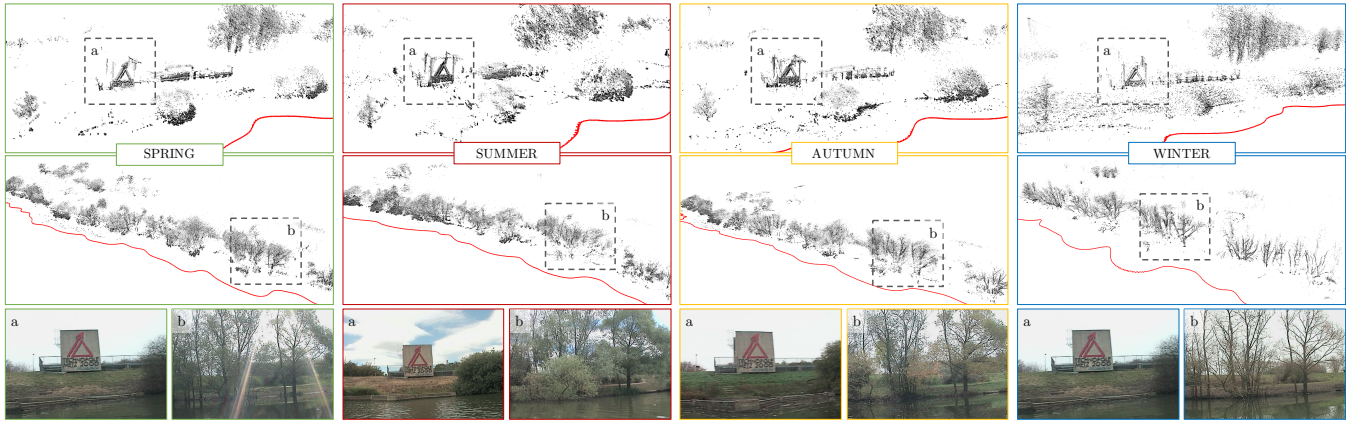


Fig. 6: **Evaluation on Symphony Lake Dataset.** The reconstructed pointclouds and example images of a human-made structure (Top) and a natural scene (Middle) are presented based on their seasons so that the structural and appearance changes across seasons can be observed. Although we merely present one sun-glare image at SPRING *b*, sun-glares exists in the most test sequences.

TABLE I: System Evaluation against Illumination Changes and Fast Camera Motion.

	Symphony Lake Dataset								Down-Sampled Symphony Lake Dataset								time	
	<i>spring</i>		<i>summer</i>		<i>autumn</i>		<i>winter</i>		<i>spring</i>		<i>summer</i>		<i>autumn</i>		<i>winter</i>		track	map
	rate	err	rate	err	rate	err	rate	err	rate	err	rate	err	rate	err	rate	error		
DSO[8]	14.2	17.4	9.3	14.7	2.5	7.7	15.9	21.7	19.9	21.0	12.7	17.8	7.2	11.1	19.4	25.7	58	93
ORB[4]	23.5	26.3	16.4	19.3	8.8	13.3	19.2	24.6	24.1	26.6	16.0	22.1	8.9	13.5	19.6	24.8	-	-
Prev[27]	4.7	9.7	4.4	9.2	2.2	6.4	8.0	12.4	10.2	14.7	7.6	11.5	7.3	11.4	14.1	18.5	105	173
Ours(Canny[31])	3.3	8.1	4.9	9.6	2.2	6.4	2.4	6.3	3.6	8.9	5.1	10.8	3.4	8.2	2.5	6.4	77	201
Ours(SE[12])	1.8	6.8	3.3	8.4	2.2	6.4	2.4	6.1	2.1	7.0	4.9	10.1	2.3	6.6	2.3	6.2	89	193
Ours(HED[13])	1.9	6.9	3.1	8.2	2.2	6.3	2.4	6.1	2.2	7.1	4.8	10.1	2.2	6.4	2.4	6.2	92	194

Rates are failure rate per sequence, averaged over 10 trials. Err is a drift rate in [cm/m]. Processing time in [ms] per frame.

generally hold more clear and uniformly distributed edges compared with those of *Summer*. Among different edge detectors, the learned edges (SE[12], HED[13]) present overall better tracking accuracy and robustness over conventional Canny edge detector, which is most likely due to the low repeatability of Canny edges in the outdoor image sequences [30]. Such degradations are also observed in the experiments in indoor operations [14].

For the evaluation on the influence of high-speed camera motions, it can be observed that both the tracking failure rates and tracking accuracy of state-of-art methods drop severely after frame sub-sampling in comparison of our proposed approach. Similar to our previous analysis, the *Winter* sequences using learned edges shows the least performance degradation compared with other approaches. It suggests that the well-distributed high-repeatability edges are essential for our proposed edge VO framework, which guarantees both the robustness against illumination changes as well as high-speed camera motions.

C. Evaluation on Regular Sequences

Besides challenging illumination- and motion-challenging dataset, we also evaluate our proposed system on regular sequences for completeness. Table. II shows the absolute trajectory errors (ATEs) after scale correction using ground truth poses using well-known KITTI [26] dataset. Not surprisingly that our proposed edge VO approaches shows stable improvements over direct DSO [8] and achieves comparable performance with indirect ORBSLAM2 [4].

TABLE II: System Evaluation on Normal Sequences.

KITTI [26]	DSO [8]	ORB [4]	Ours(Canny) [31]	Ours(SE) [12]	Ours(HED) [13]
00	16.83	16.14	18.36	16.06	16.11
01	36.32	-	32.59	22.31	21.55
02	17.08	15.58	17.72	16.47	16.52
03	3.71	3.44	4.31	3.64	3.63
04	3.01	3.05	2.93	2.11	2.03
05	13.64	12.96	13.49	13.05	13.02
06	14.13	13.35	13.44	12.54	12.57
07	9.55	10.63	11.36	8.15	8.20
08	18.31	15.43	19.35	16.24	16.21
09	13.05	12.88	12.73	11.81	11.77

VIII. CONCLUSIONS

In this work, we propose a monocular semi-direct visual odometry framework, which is a real-time capable algorithm exploiting the edge features and image gradient for illumination-robust camera motion estimation and scene reconstruction. These are obtained by joint optimization of edge alignment and image gradient error through a convergence-preserved reweighting strategy in tracking layer, a finer point correspondence refinement strategy through a fast probabilistic 1D search strategy, and joint optimization in local bundle adjustment. The proposed system successfully overcomes the partial observability issue of monocular edge mapping as well as improving the robustness of outdoor motion estimation. The experimental results indicate that our proposed system outperforms current state-of-art algorithms in terms of illumination- and motion-robustness and shows comparable performance in regular sequences.

REFERENCES

- [1] G. Klein and D. Murray, "Parallel tracking and mapping for small ar workspaces," in *Proceedings of the 2007 6th IEEE and ACM International Symposium on Mixed and Augmented Reality*. IEEE Computer Society, 2007, pp. 1–10.
- [2] H. Strasdat, J. Montiel, and A. J. Davison, "Scale drift-aware large scale monocular slam," *Robotics: Science and Systems VI*, vol. 2, no. 3, p. 7, 2010.
- [3] R. Mur-Artal, J. M. M. Montiel, and J. D. Tardos, "Orb-slam: a versatile and accurate monocular slam system," *IEEE transactions on robotics*, vol. 31, no. 5, pp. 1147–1163, 2015.
- [4] R. Mur-Artal and J. D. Tardós, "Orb-slam2: An open-source slam system for monocular, stereo, and rgb-d cameras," *IEEE Transactions on Robotics*, vol. 33, no. 5, pp. 1255–1262, 2017.
- [5] R. A. Newcombe, S. J. Lovegrove, and A. J. Davison, "Dtam: Dense tracking and mapping in real-time," in *2011 international conference on computer vision*. IEEE, 2011, pp. 2320–2327.
- [6] M. Pizzoli, C. Forster, and D. Scaramuzza, "Remode: Probabilistic, monocular dense reconstruction in real time," in *2014 IEEE International Conference on Robotics and Automation (ICRA)*. IEEE, 2014, pp. 2609–2616.
- [7] J. Engel, T. Schöps, and D. Cremers, "Lsd-slam: Large-scale direct monocular slam," in *European conference on computer vision*. Springer, 2014, pp. 834–849.
- [8] J. Engel, V. Koltun, and D. Cremers, "Direct sparse odometry," *IEEE transactions on pattern analysis and machine intelligence*, vol. 40, no. 3, pp. 611–625, 2017.
- [9] L. Kneip, Z. Yi, and H. Li, "Sdicp: Semi-dense tracking based on iterative closest points," in *Bmvc*, 2015, pp. 100–1.
- [10] Y. Zhou, L. Kneip, and H. Li, "Semi-dense visual odometry for rgb-d cameras using approximate nearest neighbour fields," in *2017 IEEE International Conference on Robotics and Automation (ICRA)*. IEEE, 2017, pp. 6261–6268.
- [11] Y. Zhou, H. Li, and L. Kneip, "Canny-vo: Visual odometry with rgb-d cameras based on geometric 3-d-2-d edge alignment," *IEEE Transactions on Robotics*, vol. 35, no. 1, pp. 184–199, 2018.
- [12] P. Dollár and C. L. Zitnick, "Structured forests for fast edge detection," in *Proceedings of the IEEE international conference on computer vision*, 2013, pp. 1841–1848.
- [13] S. Xie and Z. Tu, "Holistically-nested edge detection," in *Proceedings of the IEEE international conference on computer vision*, 2015, pp. 1395–1403.
- [14] F. Schenk and F. Fraundorfer, "Robust edge-based visual odometry using machine-learned edges," in *2017 IEEE/RSJ International Conference on Intelligent Robots and Systems (IROS)*. IEEE, 2017, pp. 1297–1304.
- [15] J.-Y. Bouguet *et al.*, "Pyramidal implementation of the affine lucas kanade feature tracker description of the algorithm," *Intel Corporation*, vol. 5, no. 1-10, p. 4, 2001.
- [16] S. Maity, A. Saha, and B. Bhowmick, "Edge slam: Edge points based monocular visual slam," in *Proceedings of the IEEE International Conference on Computer Vision*, 2017, pp. 2408–2417.
- [17] X. Wang, W. Dong, M. Zhou, R. Li, and H. Zha, "Edge enhanced direct visual odometry," in *BMVC*, 2016.
- [18] H. Alismail, B. Browning, and S. Lucey, "Robust tracking in low light and sudden illumination changes," in *2016 Fourth International Conference on 3D Vision (3DV)*. IEEE, 2016, pp. 389–398.
- [19] S. Park, T. Schöps, and M. Pollefeys, "Illumination change robustness in direct visual slam," in *2017 IEEE international conference on robotics and automation (ICRA)*. IEEE, 2017, pp. 4523–4530.
- [20] C. Forster, M. Pizzoli, and D. Scaramuzza, "Svo: Fast semi-direct monocular visual odometry," in *2014 IEEE international conference on robotics and automation (ICRA)*. IEEE, 2014, pp. 15–22.
- [21] X. Gao, R. Wang, N. Demmel, and D. Cremers, "Ldso: Direct sparse odometry with loop closure," in *2018 IEEE/RSJ International Conference on Intelligent Robots and Systems (IROS)*. IEEE, 2018, pp. 2198–2204.
- [22] S. H. Lee and J. Civera, "Loosely-coupled semi-direct monocular slam," *IEEE Robotics and Automation Letters*, vol. 4, no. 2, pp. 399–406, 2018.
- [23] J.-L. Blanco, "A tutorial on se (3) transformation parameterizations and on-manifold optimization," *University of Malaga, Tech. Rep.*, vol. 3, 2010.
- [24] A. Gaidon, Q. Wang, Y. Cabon, and E. Vig, "Virtual worlds as proxy for multi-object tracking analysis," in *Proceedings of the IEEE conference on computer vision and pattern recognition*, 2016, pp. 4340–4349.
- [25] S. Griffith, G. Chahine, and C. Pradalier, "Symphony lake dataset," *The International Journal of Robotics Research*, vol. 36, no. 11, pp. 1151–1158, 2017.
- [26] A. Geiger, P. Lenz, and R. Urtasun, "Are we ready for autonomous driving? the kitti vision benchmark suite," in *Conference on Computer Vision and Pattern Recognition (CVPR)*, 2012.
- [27] X. Wu and C. Pradalier, "Illumination robust monocular direct visual odometry for outdoor environment mapping," in *2019 International Conference on Robotics and Automation (ICRA)*. IEEE, 2019, pp. 2392–2398.
- [28] C. Pradalier and F. Pomerleau, "Multi-session lake-shore monitoring in visually challenging conditions," 2018.
- [29] G. Chahine and C. Pradalier, "Survey of monocular slam algorithms in natural environments," in *2018 15th Conference on Computer and Robot Vision (CRV)*. IEEE, 2018, pp. 345–352.
- [30] X. Wu, A. Benbihi, A. Richard, and C. Pradalier, "Semantic nearest neighbor fields monocular edge visual-odometry," *arXiv preprint arXiv:1904.00738*, 2019.
- [31] J. Canny, "A computational approach to edge detection," in *Readings in computer vision*. Elsevier, 1987, pp. 184–203.